https://doi.org/10.1016/j.energy.2023.126714

Interaction of two fully passive flapping foils arranged in tandem and its influence on flow energy harvesting

Fuwang Zhao[1,2,3#], Qian Jiang[1#], Zhaokun Wang[1], M. N. Mumtaz Qadri[1,4], Li Li[3], Hui Tang[1, 2*]

[1]*Department of Mechanical Engineering, The Hong Kong Polytechnic University, Kowloon, Hong Kong, China*
[2]*The Hong Kong Polytechnic University Shenzhen Research Institute, Shenzhen, Guangdong 518057, China*
[3]*School of Fashion and Textiles, The Hong Kong Polytechnic University, Kowloon, Hong Kong, China*
[4]*Department of Aerospace Engineering, College of Aeronautical Engineering, National University of Sciences and Technology, Risalpur, Pakistan*
[#]These authors contributed equally to this work
[*]Corresponding author: h.tang@polyu.edu.hk

ABSTRACT

We investigated the dynamics and energy harvesting performance of a novel flow-energy harvesting system that consists of two fully passive flapping foils arranged in tandem. Both experimental tests and numerical simulations were conducted to uncover the wake-foil and foil-foil interaction mechanism. The system was tested in a chord-based Reynolds number of 8.7×10^4, at various initial states and tandem distances. It was found that the aft foil was modulated and eventually locked by the wake of the flapping fore foil, leading to a stable phase difference between the two foils that is independent of the foils' initial states and varies almost linearly with the tandem distance. Within the test range, the aft foil always exhibited larger heaving and pitch velocities, extracting in average 15.2% more power than the fore foil and the single foil. The best power extraction efficiency of 19.6% was achieved by the aft foil when the two foils are separated by only one chord length, while the worst efficiency of 15.9% was achieved by the fore foil when they are separated by two chord lengths. Collectively, the two foils can achieve the best efficiency of 36.8%, greater than the doubled value (i.e., 33.4%) of the single foil's efficiency.

1. Introduction

Great effort has been made to harness energy from air or water flow to meet the energy crisis. Among others, flow-induced vibration (FIV), including vortex-induced vibration, galloping and fluttering has mostly been taken as the kinetic source of energy harvester (Abdelkefi 2015, Wang et al.2020 and Wang & Zhao 2021). Flapping foil-based energy harvesters are a type of unconventional concepts for air/water flow energy harvesting. Compared to traditional rotary turbines, they have many advantages, such as having low cut-in speeds, better filling factor, scalable, operable in shallow water and environmentally friendly. Depending on the way of actuation, these flow energy harvesters are usually operated in three different modes: the *fully active* mode where both the heaving and pitching motions are prescribed, the *semi-active* or *semi-passive* mode where one of the motions is prescribed while the other is induced by the flow, and the *fully passive* mode where both the motions are flow induced. Profound understandings have been achieved on the dynamics and energy extraction performance of single-foil systems (Xiao et al. 2014, Young et al. 2014, Wu et al.2020 and Wang et al.2020).

From the practical perspective, it is usually required to arrange flapping foil-based flow energy harvesters in arrays, so as to make the best from the flow at selected sites as well as to save the operation and maintenance costs. As the simplest configuration of harvester arrays, two-foil systems, especially arranged in tandem, are usually chosen to study the detailed foil-foil or wake-foil interactions and their influence on resulting energy harvesting. Recent works on this topic are summarized in Table 1. Through computational fluid dynamics (CFD) simulations on a fully active tandem foil system, Platzer et al. (2009a) and Ashraf et al. (2011) pointed out that

the energy extraction performance can be affected by the tandem distance and inter-foil phase difference, and the aft foil can be placed at an optimal distance with an optimal phase difference to extract maximum power for a system at given amplitudes of motion and Reynolds number. However, if compared with a single foil, both the averaged power output and efficiency per foil are reduced by around 20%, mainly due to the poor performance of the aft foil. The deteriorated performance of the aft foil was also observed by Xu et al. (2016), Liu (2017) and Ribeiro et al (2021). Meanwhile, contradicting results were also reported in Karbasian et al. (2015) and Karakas & Fenercioglu (2017) that the aft foil can attain a higher power efficiency than the fore foil due to the favorable wake-foil interactions. Broering & Lian (2012), Broering et al. (2012) and Xu & Xu (2017) further found that the best average efficiency of the aft foil can be higher than that for the single foil.

Many of the above researchers have noticed that similar aft-foil dynamics can be achieved by changing either the tandem distance or the inter-foil phase difference (Broering & Lian 2012; Broering et al. 2012; Kinsey & Dumas 2012a, 2012b; Xu & Xu 2017; Ribeiro et al. 2021). To better predict the performance of the aft foil, Kinsey & Dumas (2012a, 2012b) proposed a parameter "global phase shift" for the aft foil, Φ, which combines the tandem-distance (L) induced phase difference and the apparent inter-foil phase difference φ

$$\Phi = 2\pi \frac{fL}{U_\infty} + \varphi \tag{1}$$

U_∞ is the freestream velocity and f is the flapping frequency. Through simulating a fully active tandem foil system, they found that $\Phi = 90°$ typically leads to the optimal performance for the aft foil. However, Xu & Xu (2017) determined a quite different value, i.e., $\Phi = 160°$, for the best aft foil performance. By replacing U_∞ with an average wake velocity U_w that accounts for the velocity deficit in the fore foil's wake, Ribeiro et al (2021) proposed a modified phase shift for the aft foil called "wake phase"

$$\Phi_w = 2\pi \frac{fL}{U_w} + \varphi \tag{2}$$

They obtained an optimal wake phase of $\Phi_w = 120°$ in the so-called LEV regime where the wake of the fore foil is dominated by leading-edge vortices (LEV).

When the tandem foils are operated in the semi-active mode, usually the pitching motion is prescribed while the heaving motion is driven by the surrounding flow. Abiru & Yoshitake (2011) experimentally studied a semi-active tandem foil system. Their results showed that, if operated in antiphase ($\varphi = 180°$), both the foils showed better energy extraction efficiencies than the single foil. In contrast, if operated in phase ($\varphi = 0$), both the foils performed worse unless the tandem distance is more than $3c$ (c is the chord of the foil). Kim et al. (2015) also designed and tested a semi-active tandem foil system. They found that, with the tandem distance $L = 2c$ and phase difference $\varphi = 190°$, similar power extraction performance was observed among the fore foil, the aft foil and the single foil. However, as L increases to $4c$, the aft foil performance deteriorated due to the unfavorable wake-foil interaction. Ma et al. (2021) numerically investigated two semi-active tandem foils operating in phase. They found that in most cases the aft foil had an inferior power output induced by the unfavorable wake-foil interactions. In some cases where the favorable wake-foil interaction occurred, the aft foil showed a better performance than the single foil, but the fore foil exhibited a very poor performance. As such, the system was still not able to achieve an efficiency per foil better than that of the single foil.

The fully passive flapping foil systems can be classified into four types (named Type I to Type IV) according to their realization (Zhao et al. 2021). The Type-II system involves two foils in tandem, which realizes continuous flapping motions by interconnecting the foils with a fixed, non-zero phase difference such that the null spot of one foil coincides with the power stroke of the other. Jones et al. (2003) designed an energy harvester of such a type and achieved self-start and smooth flapping motion by operating the two foils with a tandem distance of $L = 9.6c$ and a phase difference of $\varphi = \pi/2$. Kinsey et al. (2011) designed and experimentally tested another Type II system where $L = 5.4c$ and $\varphi = \pi$. The maximum total efficiency of this tandem-foil system reached 30%, significantly larger than 20% obtained from the corresponding single-foil system.

Table 1. Summary of studies on tandem flapping-foil based flow-energy harvesters

Mode	Authors	*L/c*	*φ/π*	Re (×10^4)	Method	Power conversion efficiency			
						Single	**Fore**	**Aft**	**Total**
Fully active	Platzer et al.(2009a)	2 ~ 6	0 ~ 0.5	2	CFD	31%	-	-	52%
	Ashraf et al. (2011)	2 ~ 6	0 ~ 1	4	CFD	34%	38%	16%	54%
	Broering & Lian (2012)	1.1 ~ 2	0 ~ 1	0.5	CFD	-	-	-	-
	Broering et al. (2012)	2	0 ~ 1	1	CFD	-	-	-	-
	Kinsey & Dumas (2012a)	5.4	1	50	CFD	38.7%	35.9%	28.3%	64.1%
	Kinsey & Dumas (2012b)	3.6 ~ 7.5	-1 ~ 1	50	CFD	38.7%	35.9%	28.3%	64.1%
	Karbasian et al. (2015)	2.55	0	40 ~ 90	CFD	25%	-	-	-
	Xu et al. (2016)	4.5 ~ 6.3	1	39.6	CFD	35%	30%	22%	53.8%
	Liu (2017)	5.4	-0.5	50	CFD	34%	33%	27%	60%
	Xu & Xu (2017)	5.4	-1 ~ 1	50	CFD	23%	23%	24%	46%
	Pourmahdavi et al. (2019)	5.4	1	50	CFD	34%	33%	27%	60%
	Karakas & Fenercioglu (2017)	2	-1 ~ 1	1	Exp	17%	-	17.8%	-
	Ribeiro et al (2021)	6 ~ 12	-1 ~ 1	3 (Exp) 0.1 (CFD)	Exp & CFD	-	23.5% (Exp) 26.5% (CFD)	14.5% (Exp) 14.5% (CFD)	38% (Exp) 41% (CFD)
Semi-active	Abiru & Yoshitake (2011)	1 ~ 10	0, 1	5	Exp	19%	21.6%	21.3%	42.9%
	Kim et al. (2015)	2 ~ 4	0.5	78 ~ 92	Exp & CFD	17%	15.5%	17.0%	32.5%
	Ma et al. (2021)	2 ~ 5	0	100	CFD	22%	-		43.7%
Fully passive	Jones et al. (2003)	9.6	0.5	2.2	Exp	-	-	-	10%
	Kinsey et al. (2011)	5.4	1	41~ 48	Exp	20%	-	-	30%
	Xu et al. (2017)	5.4	1	26 ~ 38	Exp	19.8%	-	-	29.2%
	Ma et al. (2019)	3 ~ 6	0	100	CFD	23.7%	18.5%	16.1%	34.6%
	Xu et al. (2019)	3	-1 ~ 1	10 ~ 12	Exp & CFD	25.2%	-	-	36.6%

Different from Type II systems which have only one degree of freedom (DOF) for tandem foils, Type IV systems utilize a group of heaving and pitching limiters to achieve continuous flapping motions, each foil having two DOFs, i.e., the pitching and heaving motions are independent (Its kinematics is depicted later in Fig. 5). Initially proposed by Platzer and colleagues (2009a, 2009b, 2009c), this novel concept has recently been studied in a systematical way on a single foil system about its detailed fluid-structure interactions (FSI), effects of key parameters, and search of best energy harvesting performance (Mumtaz Qadri et al. 2020; Zhao et al. 2021). If two such foils are arranged in tandem, the total four DOFs in the system could generate very rich dynamics that makes impacts on the resulting energy harvesting performance. This motivates us to conduct the present research, with the focus placed on the wake-foil and foil-foil interactions. Both experimental and numerical investigations are performed to provide complementing data.

The paper is organized as follows: In Section 2, the design of the Type IV fully passive tandem foil system and its experimental and numerical methods are introduced. The dynamics and power extraction performance of this system are presented and discussed in Section 3. A summary from this study is given in Section 4.

2. Methodology

2.1 Experimental setup

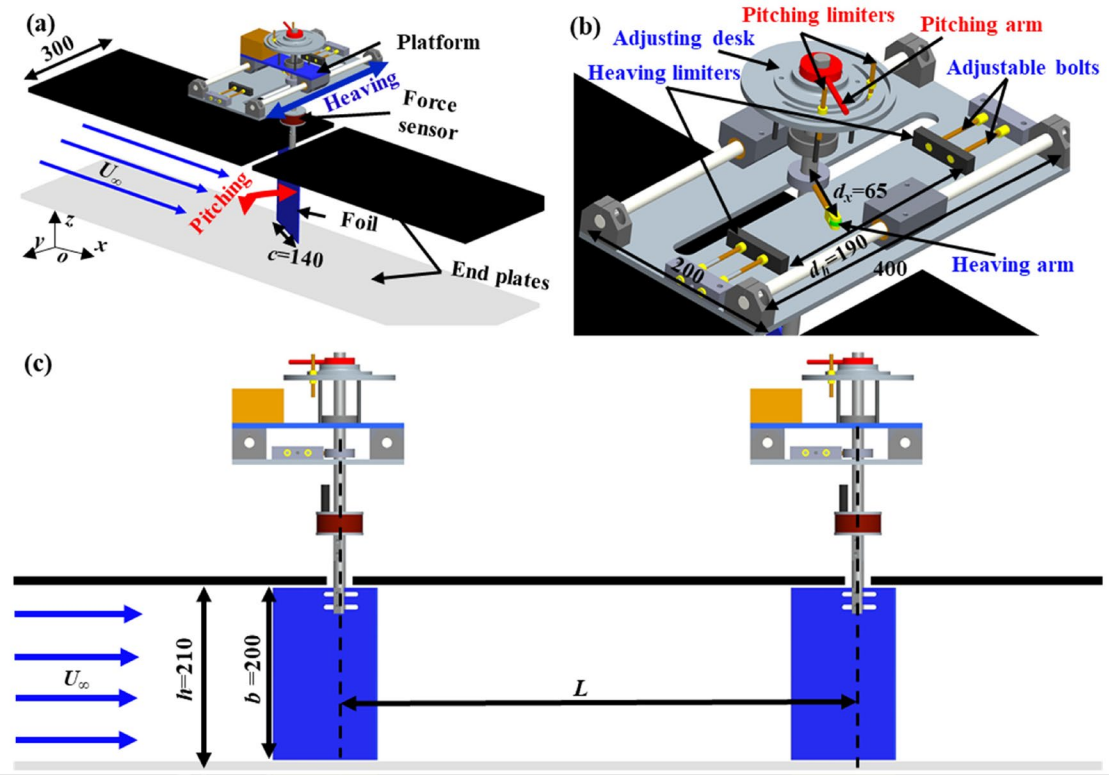

Fig. 1 Schematic of the water channel test rig. (a) isometric view of the setup with a single foil, where a laboratory-fixed coordinate system is defined; (b) close-up view of the top part of the single foil; and (c) two foils in tandem. All dimensions are in mm.

The test rig is schematically shown in Fig. 1 and its main parameters are listed in Table 2. Two identical flapping foil systems are arranged in tandem along a water channel of 0.3 m wide, 0.6 m high, and 2 m long, as shown in Fig. 1(c). Each foil system is equipped with a flat foil of chord c = 140 mm, span b = 200 mm, and mass m_1 = 0.38 kg, which is mounted underneath a heaving platform through a long shaft located at 0.6c from the foil's leading edge. Driven by a water flow of speed U_∞ = 0.62 m/s (corresponding to a chord-based Reynolds number 8.7×10^4), the foil can undergo both heaving (together with the platform) and pitching (about the long shaft) motions. The ranges of these two motions can be pre-set by adjusting the heaving and pitching arm-limiter

mechanisms, as depicted in Fig. 1(b). The total mass of the heaving part is around m = 4.25 kg, and the moment of inertia of the rotating part is about $I = 9.62\times10^{-4}$ kg-m^2. To eliminate three-dimensional effects, the lower end of the foils is only 5 mm from the bottom of the water channel, whereas end plates are deployed at the upper end of the foils, also leaving a 5 mm gap. The hydrodynamic forces/torque experienced by the foils were measured using a six-axis force sensor (ATI Mini-40) installed in the shaft (see Fig. 1(a)) with a sampling rate of 2,000 Hz. Meanwhile, the foils' motions were recorded using a high-speed camera (Photron Mini UX100) operating at 125 fps. Both the devices were interfaced with NI DAQ cards and synchronized in LabVIEW software. For more details about the test rig and the relevant measurements, readers are referred to our previous works (Mumtaz Qadri et al. 2020; Zhao et al. 2021).

Table 2 Parameters of the test rig used in numerical simulation and experiments

Foil shape	Flat plate
Chord length of the foil (c)	0.14 m
Span of the foil (a)	0.2 m
Thickness of the foil (b)	0.005 m
Mass of the foil (m_1)	0.378 kg
Pivot location from leading edge (x_p)	0.084 m (0.6c)
Heaving amplitude (h_0)	Variable, slightly larger than d_h/2
Pitching amplitude (θ_0)	40°
Mass related heaving motion (m_h)	4.25kg
Moment of inertia (I)	9.62×10^{-4} kg.m^2
Distance between heaving limiters (d_h)	0.19 m (1.36c)
Distance between heaving limiter and sweep plane (d_x)	0.065 m (0.16c)
Damping coefficient for heaving direction (c_h)	0.005 N-s/m
Damping coefficient for pitching direction (c_θ)	0.04 N-m-s/rad
Reynolds number (Re)	8.7×10^4

As reported in our previous study (Zhao et al. 2021), the dynamics of a single foil can generally be divided into two phases, i.e., the "pure heaving phase" and the "stroke-reversal phase". Take the upstroke as an example, the pure heaving phase begins when the pitching arm starts to touch the lower pitching limiter from the previous stroke reversal (Fig. 2(a)). Confined by this pitching limiter through a non-zero reaction force F_{pl}, the foil maintains its maximum pitching angle during the entire phase, i.e., $\theta = +\theta_0$ and $\dot{\theta} = 0$. With such a large pitching angle, the foil is pushed upward along the linear guide by the hydrodynamic heaving force F_h. This pure heaving ends when the foil starts to touch the upper heaving limiter. At this instant, the foil's heaving displacement is $h = d_h/2 - d_x \tan\theta_0$, where d_h and d_x are the distance between the two heaving limiters and the streamwise distance between the sweep plane of pivot axis and the heaving limiters, respectively. This displacement defines the boundary between the pure heaving phase and the subsequent stroke-reversal phase.

After touching the upper heaving limiter, the foil is forced to rotate anticlockwise and leaves the confining pitching limiter (so that $F_{pl} = 0$). As such, it enters the stroke-reversal phase, in which the foil keeps rotating from $+\theta_0$ to $-\theta_0$ until it touches the upper pitching limiter (Fig. 2(b) and 2(c)) to start the next pure-heaving phase. Depending on whether the foil has contact with the heaving limiter or not, the stroke-reversal phase can be further divided into two stages: the "sliding stage" and the "free stage". In the sliding stage as shown in Fig. 2(b), the foil remains contact with the upper heaving limiter. The latter then exerts a non-zero reaction force F_{hl} on the foil, forcing the foil to rotates anticlockwise about its pivot axis. During this process the heaving arm keeps sliding on the heaving limiter. The foil's instantaneous heaving displacement can be determined as $h = d_h/2 - d_x \tan\theta$. Note that the pitching angle θ may become negative due to the inertia so that the heaving force and pitching moment reverse their directions.

The sliding stage ends when the foil starts to leave the upper heaving limiter (so that $F_{hl} = 0$) due to the reversed hydrodynamic force/moment. After that, the foil continues rotating anticlockwise until it touches the upper pitching limiter to reach its maximum allowed negative pitching angle $-\theta_0$ (see Fig. 2c). This defines the

free stage, in which the foil has no contact with any limiter, i.e., $F_{hl} = F_{pl} = 0$.

The same pure-heaving and stroke-reversal phases will repeat during the subsequent downstroke. As such, a complete flapping cycle consists of two pure-heaving phases and two stroke-reversal phases.

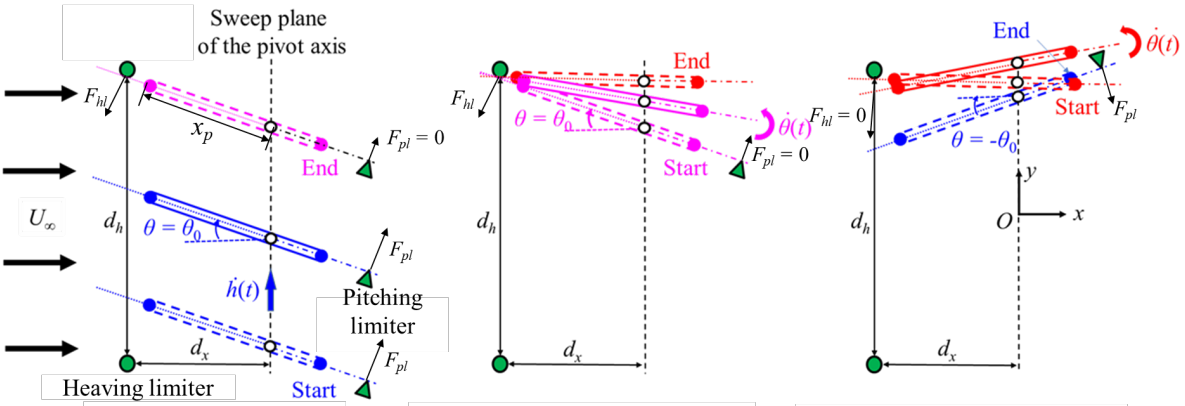

Fig. 2 Schematics showing the kinematics of a single foil in a half flapping cycle: (a) the pure heaving phase (in blue), (b) the sliding stage of the stroke-reversal phase (in pink), and (c) the free stage of the stroke reversal phase (in red). d_h is the distance between the two heaving limiters, d_x is the distance between the heaving limiters and the sweep plane of the foil's pivot axis. x_p defines the distance of the pivot axis from the foil's leading edge. F_{hl} is the reaction force of the heaving limiter on the heaving arm and F_{pl} is the reaction force of the pitching limiter on the pitching arm.

2.2 CFD simulations

To supplement the experiments by providing detailed flow information around the flapping foils as well as to extend the parameter space, CFD investigations were conducted using ANSYS Fluent. The computational domain and boundary conditions are sketched in Fig. 3. A uniform flow of speed U_∞ enters the left boundary, interacts with the two flapping foils, and leaves the right boundary far downstream with a constant pressure. The upper and lower boundaries are treated as walls with no-slip boundary condition. As such, this computational domain replicates the laboratory conditions in the water channel. To address the challenges caused by the foils' large-amplitude heaving and pitching motions, a set of overset mesh (orange zones in Fig. 3) was applied around each foil, which translates/rotates with the foil and exchanges flow information with the fixed background mesh. The total number of meshes is about 3×10^5. The meshes near the foils and walls were refined so that $y^+ \approx 1$ at this first grid layer.

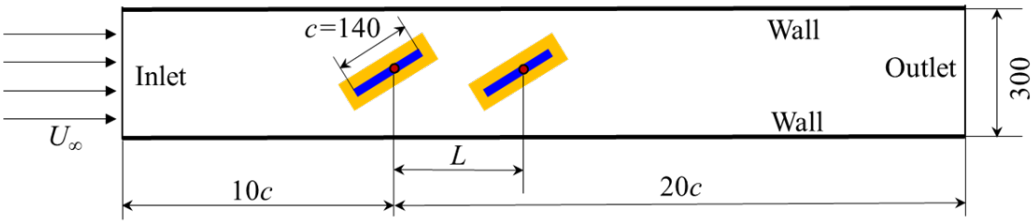

Fig. 3 Computational domain and boundary conditions used in the CFD study. The two blue rectangles represent the flapping foils, and the orange zones denote the overset mesh. All dimensions are in mm.

A user defined function (UDF) was implemented to coordinate the simulations. As described in the flow chart in Fig. 4, the simulation starts from the pure heaving phase, which is subsequently followed by the sliding stage and the free stage. The classification criteria and boundaries of these phases/stages can be read in Fig. 4. In each phase/stage, the FSI module is called, in which the mesh is updated first according to the latest foil position, the fluid flow is simulated by solving the Reynolds-Averaged Navier-Stokes (RANS) equations, and then the foils' kinematics is obtained by solving the following equations based on the Newton's second law.

For heaving motion: $m\ddot{h} + F_{hl}\cos\theta + c_h\dot{h} = F_h$ (3)

For pitching motion: $I\ddot{\theta} + F_{hl}d_x\sec\theta + c_\theta\dot{\theta} = M_\theta$ (4)

where h is the heaving displacement. F_h and M_θ are hydrodynamic force and moment determined by the fluid solver, respectively. c_h and c_θ are the damping coefficients for heaving and pitching motions, respectively, which were determined through simple tests on the test rig. For the flow simulation, the second-order upwind scheme and the first-order implicit scheme were implemented for spatial and temporal discretization, respectively, and the turbulence was modeled using the SST k-ω model.

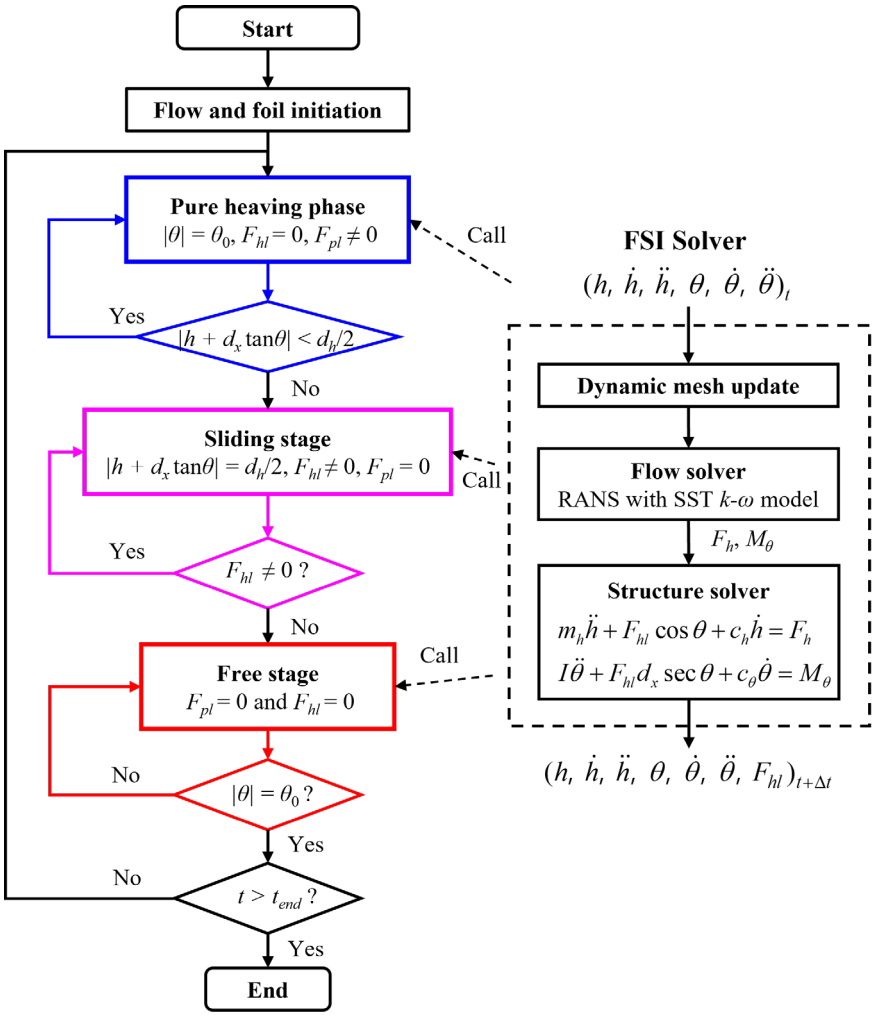

Fig. 4 Flowchart of CFD simulations where a UDF is implemented to update the dynamic mesh and call the flow and structure solvers in the pure heaving phase (in blue), the sliding stage (in pink) or the free stage (in red).

To validate this CFD framework, we simulated the flow around a fully active flapping foil, which has also been simulated by Kinsey & Dumas (2008) and Wu et al. (2014). The foil has a NACA0015 profile and flaps with a heaving amplitude of one chord, a pitching amplitude of 76.3°, and its pitching axis being located one third of the chord from the leading edge, and at a Reynolds number of 1,100. The good agreements in the evolution of hydrodynamic forces experienced by the foil shown in Fig. 5, in the vorticity and pressure contours exhibited in Fig. 6, and in the mean force coefficients and power conversion efficiencies listed in Table 3 confirm that the current CFD framework is capable of simulating this type of FSI problems. The confidence in our CFD framework can be further reinforced through comparisons with the experimental data obtained in the present study, which will be presented in Sec. 3.

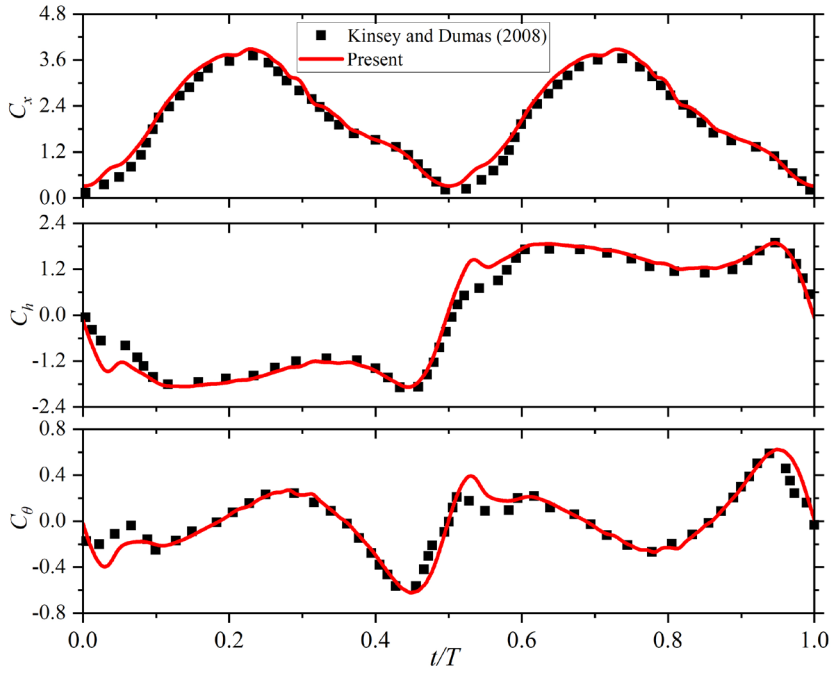

Fig. 5 Comparison of the hydrodynamic forces experienced by a fully active flapping foil: (a) streamwise force coefficient C_x; (b) heaving force coefficient C_h; and (c) pitching moment coefficient C_θ

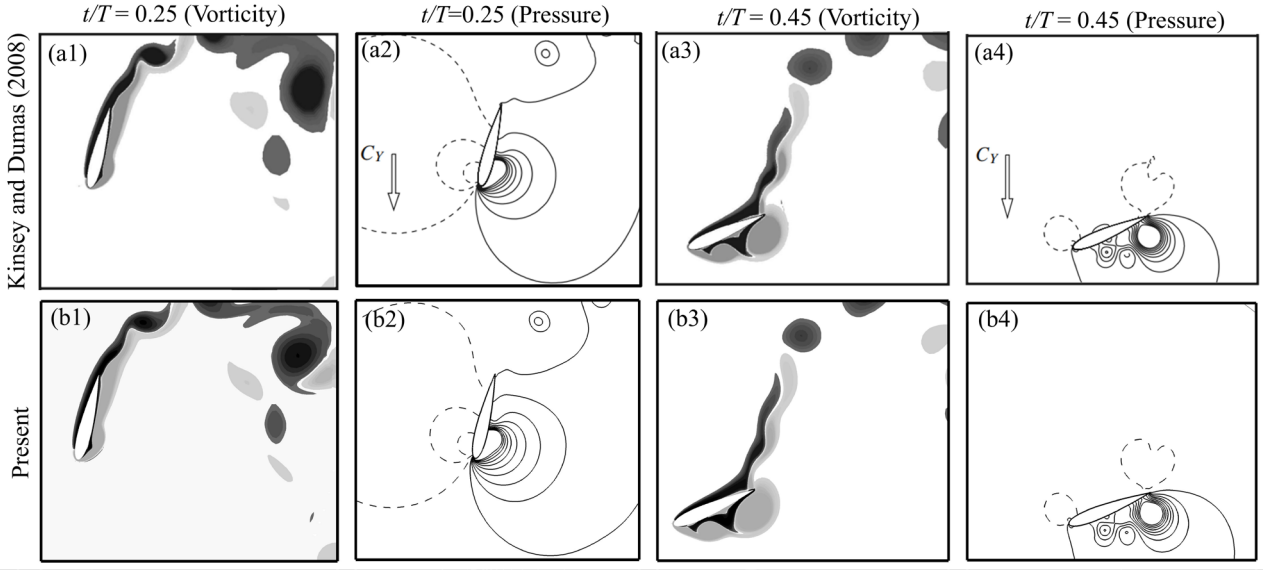

Fig. 6 Comparison of vorticity and pressure contours around a fully active flapping foil at selected instants.

Table 3. Comparison of hydrodynamic forces and power conversion efficiencies of a fully active flapping foil system

Author	Mean horizontal force coefficient, $\bar{C}_x$	Mean vertical force coefficient, $\bar{C}_y$	Mean pitching moment coefficient, $\bar{C}_m$	power conversion efficiency, η
Kinsey and Dumas (2008)	2.02	1.94	0.66	33.9%
Wu *et al.* (2014)	2.11	1.97	——	34.7%
Present	2.08	2.02	0.67	34.4%

2.3 Data analysis

In our system, the flow energy can be harvested from both the heaving and pitching motions of the flapping foil. Hence, the total power P is simply the summation of these two parts

$$P = P_h + P_\theta = F_h\dot{h} + M_\theta\dot{\theta} \tag{3}$$

where P_h and P_θ are the heaving power and pitching power, respectively, F_h and M_θ are the heaving force and pitching moment, respectively, and $\dot{h}$ and $\dot{\theta}$ are the heaving velocity and pitching velocity, respectively. These powers and forces can be nondimensionalized accordingly using the foil and fluid properties

$$C_p = C_{ph} + C_{p\theta} = \frac{F_h\dot{h}}{\rho U_\infty^3 bc/2} + \frac{M_\theta\dot{\theta}}{\rho U_\infty^3 bc/2} = C_h\frac{\dot{h}}{U_\infty} + C_\theta\frac{\dot{\theta}c}{U_\infty} \tag{4}$$

where C_{ph} and $C_{p\theta}$ are the heaving power coefficient and pitching power coefficient, respectively, C_h and C_θ are the heaving force coefficient and pitching moment coefficient, respectively, and ρ is the fluid density.

Note that, the powers, forces and velocities appearing in Eqs. (3) and (4) are all time-dependent. Their experimental data presented in the following sections are all phase averaged over at least 50 flapping cycles. To evaluate the system's overall performance, the time-averaged power coefficient, $\overline{C}_p$, can be evaluated as

$$\overline{C}_p = \overline{C}_{ph} + \overline{C}_{p\theta} = \frac{1}{T}\int_t^{t+T}\left(C_{ph} + C_{p\theta}\right)dt \tag{5}$$

where T is the flapping cycle, and the over bar denotes time averaged quantities. The system's energy extraction efficiency, η, is defined as the ratio of the mean power to the total energy available for extraction.

$$\eta = \frac{\overline{P}}{\rho U_\infty^3 bh_0} = \frac{c}{2h_0}\overline{C}_p \tag{6}$$

where h_0 is the heaving amplitude of the foil.

3.Results and Discussion

3.1. Performance of single foil

To provide a benchmark for the tandem-foil system, the dynamics and energy harvesting performance of a single-foil system are briefly introduced here, which have been systematically studied in our previous works (Mumtaz Qadri et al. 2020; Zhao et al. 2021). The evolution of the foil's dynamics and power extraction over a flapping cycle are shown in Fig. 7, under a selected flow condition with the water speed $U_\infty = 0.62$ m/s, the foil's pivot axis location $x_p = 0.6c$, the pitching amplitude $\theta_0 = 40^o$, the distance between the two heaving limiters $d_h = 1.36c$ and the streamwise distance between the sweep plane of pivot axis and the heaving limiters $d_x = 0.46c$. When the system is in the pure heaving phase (with the white background), the pitching angle is fixed at the pitching amplitude θ_0 (Fig. 7(a)). As such, the pitching velocity $\dot{\theta}$ remains zero (Fig. 7(d)), resulting in zero power extraction, i.e., $C_{p\theta} = 0$ (Fig. 7(b)). Only undergoing the heaving motion, the foil keeps its heaving velocity $\dot{h}$ increasing until the next phase (Fig. 7(c)). Since the heaving force C_h is also in the same direction, the heaving motion always extracts power in this phase, i.e., $C_{ph} > 0$, as confirmed in Fig. 7(b).

When the foil enters the sliding stage (with the light grey background), its pitching angle starts to change dramatically owing to the torque collectively generated by the heaving limiter and the system inertia. However, the pitching velocity and the pitching moment are in opposite directions, resulting in negative pitching power, i.e., $C_{p\theta} < 0$, in almost the entire sliding stage (Fig. 7(b)). Meanwhile, the foil's heaving velocity reduces continuously due to the reaction force from the heaving limiter, while the heaving force changes its direction as a result of the foil rotation. Consequently, the heaving motion extracts power (i.e., $C_{ph} > 0$) roughly in the first half of the sliding stage, while it consumes energy in the second half ($C_{ph} < 0$), as revealed in Fig. 7(b).

When the system enters the free stage (with the dark grey background), the foil's pitching angle continues changing till it touches the opposite pitching limiter. Since the pitching velocity and the pitching moment are in the same direction, the pitching motion extracts power, i.e., $C_{p\theta} > 0$ (Fig. 7(b)). In this stage, the heaving force makes the foil revert its heaving direction, resulting in the consumption of flow power in the first half and the

power extraction in the second half.

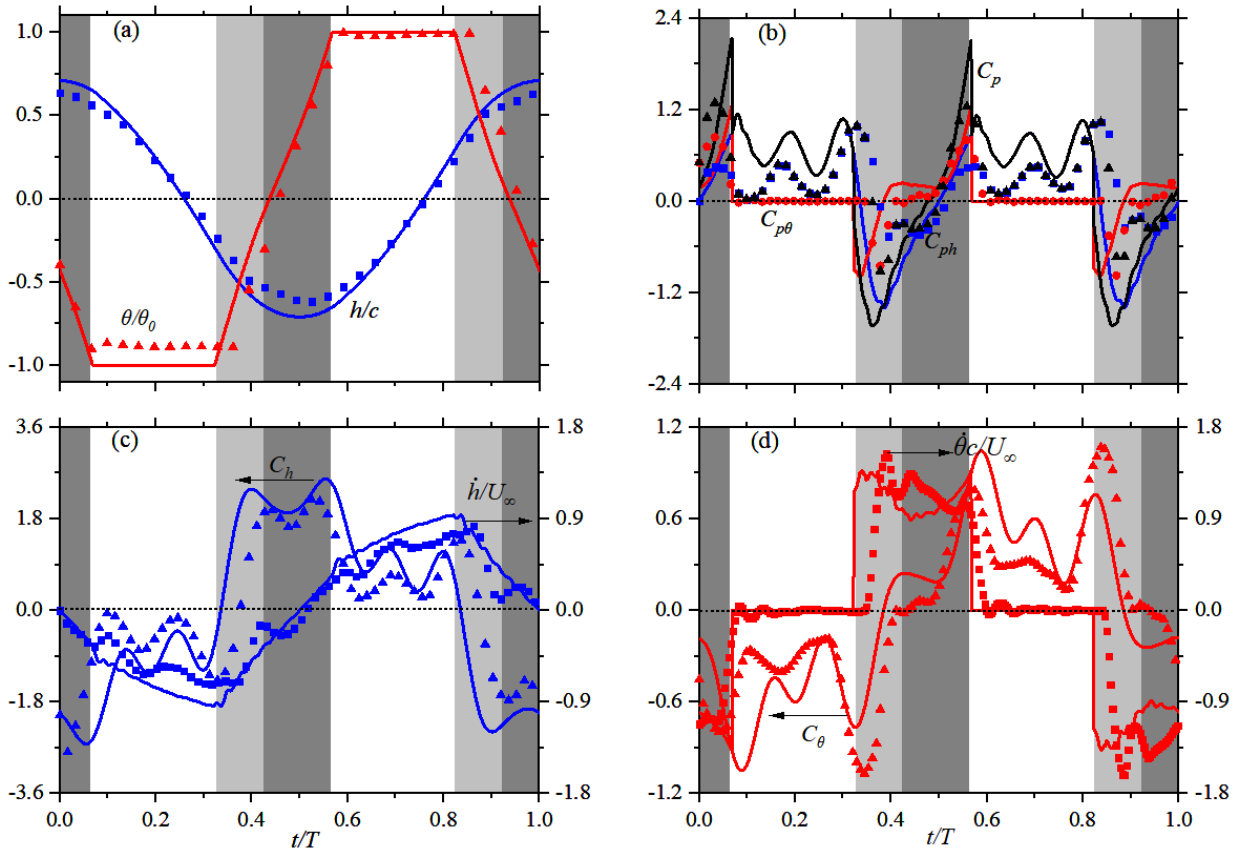

Fig. 7 Dynamics and power extraction performance of a single foil system: one-cycle evolution of the foil's (a) heaving and pitching displacements, (b) power coefficients, (c) heaving force coefficient and velocity, and (d) pitching moment coefficient and velocity, where $U_\infty = 0.62$ m/s, $x_p = 0.6c$, $\theta_0 = 40°$, $d_h = 1.36c$ and $d_x = 0.46c$. The experimental and simulation results are plotted in scatter and lines, respectively. Blue color denotes heaving related quantities, red color denotes pitching related quantities, and black color denotes the total power coefficient. White, light grey and dark grey backgrounds define the pure-heaving phase, the sliding stage of the stroke reversal phase, and the free stage of the stroke reversal phase, respectively, based on the simulation data.

The time-averaged power coefficients and overall power extraction efficiency were calculated and listed in Table 4. It clearly shows that both the heaving and pitching motions can contribute to flow energy harvesting. However, significantly more energy is harvested from the heaving motion than from the pitching motion. This is different from what has been reported in our previous works, where both motions contribute almost equally (Mumtaz Qadri et al. 2020; Zhao et al. 2021). The reason behind this change is because in the current test rig a smaller distance was adopted between the heaving limiters and the sweep plane of the pivot axis, i.e., $d_x = 0.46c$, compared to previous $0.75c$. This modification is based on our understanding obtained from Zhao et al. (2021). That is, reducing d_x can result in the increase of pure heaving time, hence leading to more heaving power, which, compared to the pitching power mainly extracted during the stroke reversal, is more convenient to extract in practice. As listed in Table 4, the overall power extraction efficiency is around $\eta = 15.1\%$, corresponding to a mean power output of 0.67 W.

CFD simulations were also conducted for this case for further validation, as represented by the solid lines in Fig. 7 and the mean values listed in Table 4. It seems that CFD-predicted dynamics and power extraction performance generally agree with the experimental measurements, which further reinforces our confidence in the CFD framework. However, there are some differences, especially in the magnitudes of force and pitching moment and the resulting power coefficients. These discrepancies are probably due to the ignorance of collision and friction between the foil and the limiters and the use of constant damping in the simulations, as well as the

imperfection of experiments. Nevertheless, these discrepancies do not affect the capture of main dynamics of the tandem foils as will be revealed and discussed in the following sections.

Table 4 Time-averaged power extraction performance of the single foil system

Method	f (Hz)	$\bar{C}_{ph}$	$\bar{C}_{p\theta}$	$\bar{C}_p = \bar{C}_{ph} + \bar{C}_{p\theta}$	η
Exp	0.82	0.16	0.042	0.202	15.1%
CFD	0.87	0.19	0.045	0.235	16.7%

3.2 Effect of initial states

When two foils are placed in tandem, their initial states including the position and orientation may influence the dynamics of both foils. To study this influence, these two foils are separated by $L = 2c$ and simultaneously released with eight selected initial states as listed in Table 5. That is, the foils are initially released around either the upper heaving end, $h = d_h/2$, the lower heaving end, $h = -d_h/2$, or at the channel centerline, $h = 0$, and their initial pitching angles are either θ_0 or $-\theta_0$. By considering the symmetry of system's kinematics and singling out several obviously non-working configurations (e.g., the case with $h = d_h/2$ and $\theta = \theta_0$), these eight cases cover all possible combinations. It is found that, regardless the initial state, the two foils can always reach the same final state: nearly antiphase motions, i.e., $\varphi \approx \pi$. This is clearly evidenced in both the CFD results (Fig. 8) and the experimental results (Fig. 9(a), multimedia view).

Table 5. All possible combinations for initial states of the tandem foils separated by $L = 2c$

Combination	Group	1	2	3	4	5	6	7	8
Fore foil	h_1	0	0	0	0	$-d_h/2$	$-d_h/2$	$-d_h/2$	$-d_h/2$
	θ_1	$-\theta_0$	$-\theta_0$	$-\theta_0$	$-\theta_0$	θ_0	θ_0	θ_0	θ_0
Aft foil	h_2	0	0	$-d_h/2$	$d_h/2$	$-d_h/2$	0	0	$d_h/2$
	θ_2	$-\theta_0$	θ_0	θ_0	$-\theta_0$	θ_0	θ_0	$-\theta_0$	$-\theta_0$
Exp	f	0.81 ± 0.02hz ($f^* = fc/U_\infty = 0.183 \pm 0.005$)							
	φ	$(1.04 \pm 0.12)\pi$							
CFD	f	0.855hz ($f^* = 0.197$)							
	φ	1.194π							

The independence of the tandem foils' motions on their initial states was also confirmed at other tandem distances (e.g., see the videos in Figs. 9(b) and 9(c) (Multimedia views) for the $L = 3c$ and $4c$ cases, respectively). Furthermore, it was found that, independent of the initial state, the final phase difference φ between the tandem foils varies almost linearly with the distance L, as revealed by both the experimental and CFD results presented in Fig. 9.

The above findings suggest that the aft foil can be "captured" by the wake of the fore foil, leading to a phase difference φ that is independent of the initial phases. That means the final phase shift of the aft foil relative to the fore foil only depends on the tandem distance L, or in other words, φ is induced by L through the wake-foil interaction. Combining this observation with the "wake phase" Φ_w defined in Eq. 2 and assuming Φ_w is independent of L, one can get $\Phi_w = 0$ for the aft foil in all cases. As such, a simple relationship between φ and L can be derived from Eq. 2 as $\varphi/2\pi = fL/U_w$ (Note that, although using the same variable φ, the phase difference used in this study has an opposite sign with the phase shift defined in Eqs. 1 and 2). Let f be the flapping frequency of a single foil, i.e., $f = f_s = 0.86$ Hz (read from the CFD results in Table 5). Using the slope of fitted data (i.e., 0.255) in Fig. 10, the averaged wake velocity can be estimated as $U_w = 0.478$ m/s, about 77% of the freestream speed U_∞. On the other hand, if U_∞ is used to estimate the "global phase shift" in Eq. 1, data fitting in Fig. 10 gives $\Phi = -1.35 \pm 0.13$ rad or $-77.5° \pm 7.7°$, which is also independent of L.

Both Φ and Φ_w values derived from the present study are quite different from those obtained from fully active tandem foil system, e.g., $\Phi = 90°$ in Kinsey & Dumas (2012a, 2012b), $\Phi = 160°$ in Xu & Xu (2017), and

Φ_w = 120° in Ribeiro et al. (2021), which is not surprising because the present fully passive system cannot deliberately pursue optimal phase differences for best performance.

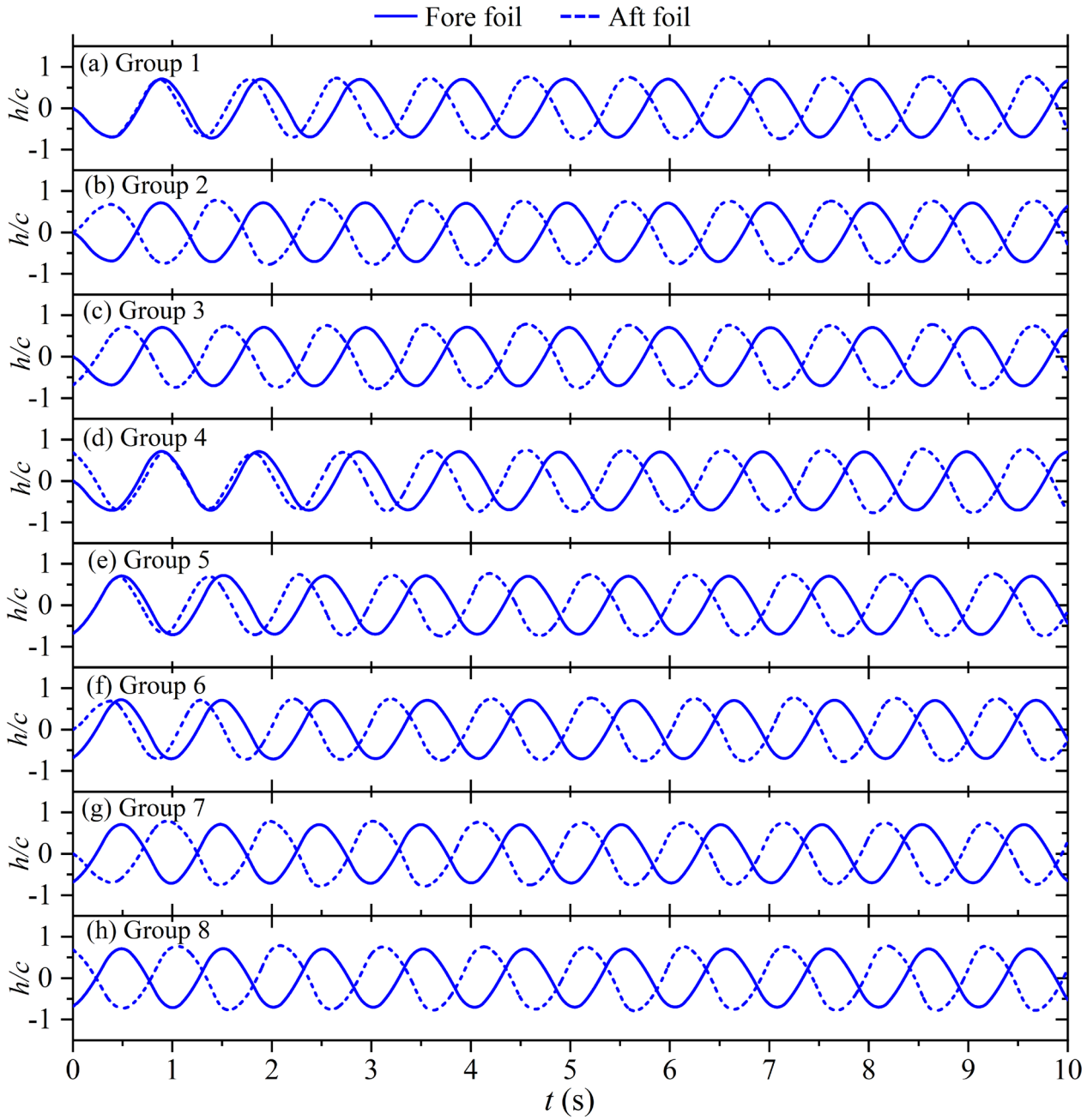

Fig. 8 Evolution of simulated heaving displacements when the tandem distance is fixed at $L = 2c$, but under various initial conditions as listed in Table 4.

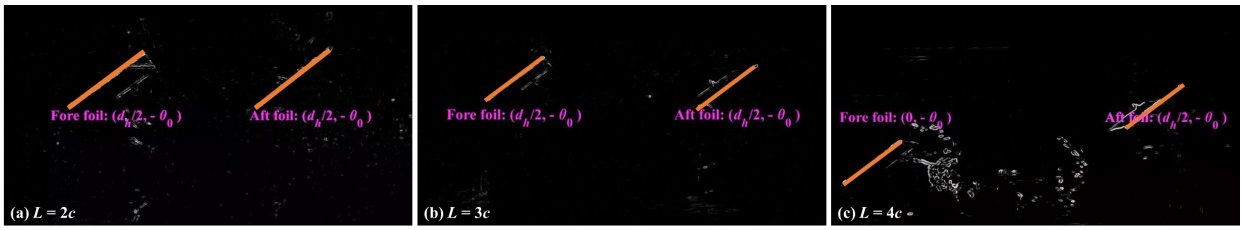

Fig. 9 Kinematics of the tandem foils after being released with selected initial conditions as listed in Table 4: (a) $L = 2c$; (b) $L = 3c$; (c) $L = 4c$. (Multimedia views, corresponding videos can be found in supplementary materials)

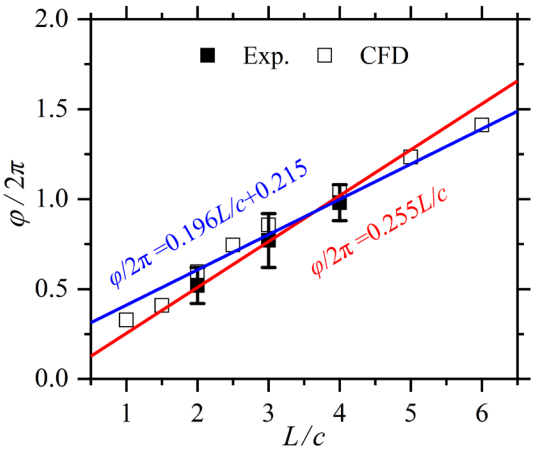

Fig. 10 Variation of the steady-state phase difference between the tandem foils against the tandem distance. The red and blue lines denote the data fitting for the "wake phase" $\Phi_w = 0$ and the "global phase shift" $\Phi = -1.35$, respectively.

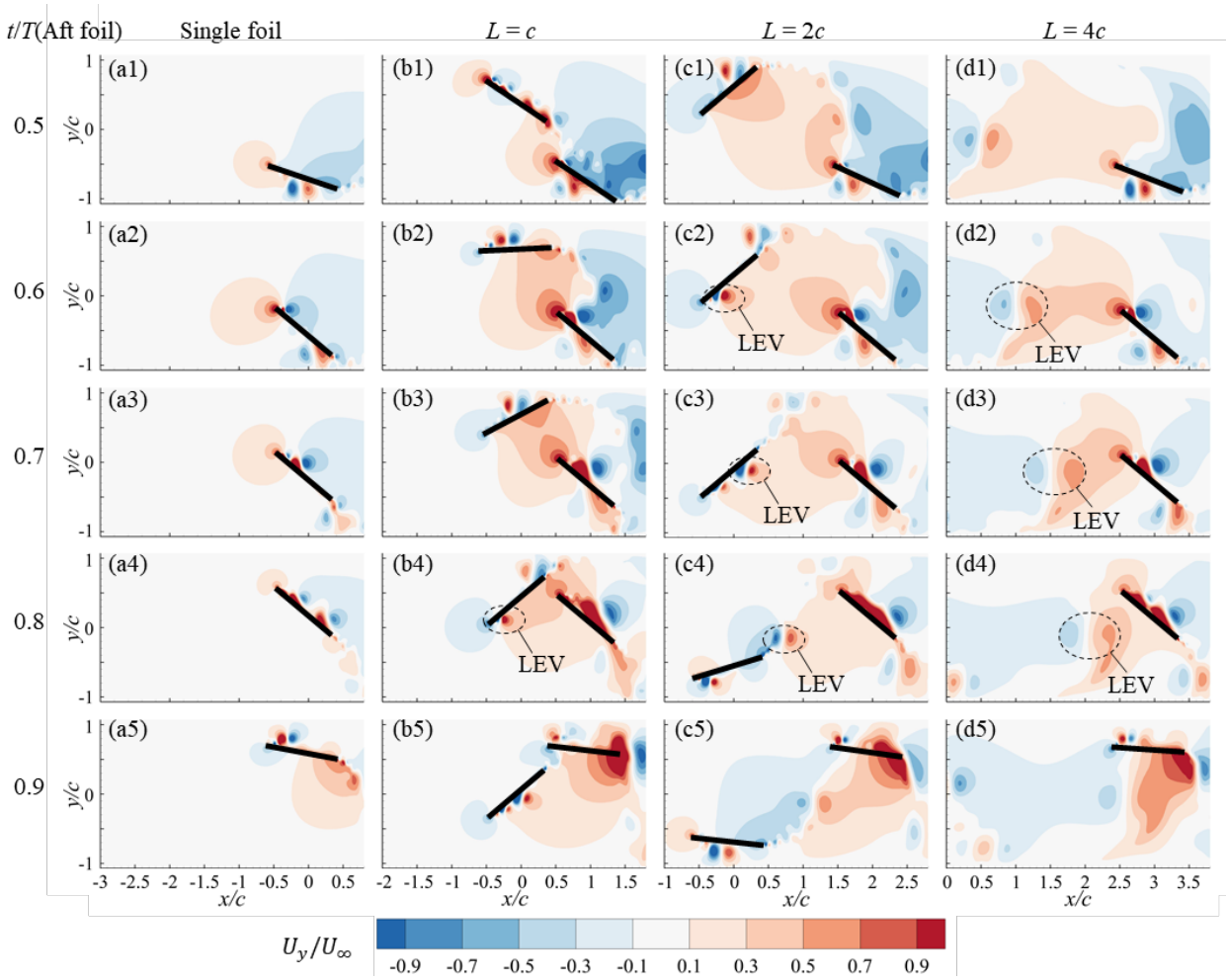

Fig. 11 Contours of transverse velocity U_y of foils over a half cycle.

To explore the wake capture mechanism, we compare the y-velocity contours for the single and $L = c$, $2c$ and $4c$ cases at selected instants during the aft foil's upstroke, as shown in Fig. 11. In the $L = 2c$ case, it is seen from Figs. 11(c2) to (c4) that a vortex shed from the leading edge of the fore foil convects towards the aft foil when the latter heaves up to cross the channel's centerline with its maximum pitching angle θ_0. This convecting leading-edge vortex (LEV) induces a stronger upward flow just upstream of the aft foil, as compared with the single foil case, hence pushing the aft foil in its heaving direction. The same is also observed in the $L = 4c$ case,

as evidenced in Figs. 11(d2) to (d4). These observations reveal that the kinematics of the aft foil is modulated and eventually locked up by the LEV generated from the fore foil. As such, the phase of the aft foil at the steady state is independent of its initial state. Instead, it is mainly related to the tandem distance L, through which the fore foil's LEV propagates.

Through this wake-foil interaction, the fore foil periodically does positive work on the aft foil via its propagating LEV, making the latter heave and pitch faster and hence leading to larger inertial forces. As the consequence, the aft foil generally exhibits a heaving amplitude about 6% larger than the fore foil, as revealed in Fig. 12(b). This difference in kinematics can also be clearly read from other detailed results shown in Sec. 3.4, which greatly affects (actually improves) the aft foil's power extraction performance.

Due to the extremely short tandem distance, the $L = c$ case (Fig. 11(b)) shows a bit different wake-foil interaction from the other two cases. In this case, in addition to the LEV generated from the fore foil, a high-momentum flow "ejected" from the fore foil through its fast anti-clockwise rotation also contributes to the lock-up of the aft foil, which will be evidenced later in Fig. 17(b3) by the sudden high pressure appearing at the pressure side of the aft foil at $t/T = 0.8$.

3.3 Two-way interactions

The interaction between the tandem foils is not just one-way, i.e., the aft foil is influenced by the fore foil's wake while the fore foil behaves like the single foil. As the tandem distance is relatively small, i.e., $L < 3c$, the fore foil's dynamics can also be affected by the aft foil. This, on one hand, is confirmed by the variation of synchronized flapping frequency $f^* = fc/U_\infty$ for both foils as shown in Fig. 12(a), where f deviates from the single foil's flapping frequency f_s^* (= 0.197) at $L < 3c$. Specifically, f^* decreases first from its maximum value (0.2) at $L = c$ to its minimum value (0.193) at $L = 2c$, and then gradually approaches to f_s^* roughly at $L = 3c$. On the other hand, the interaction also influences the fore foil's swept distance when $L < 3c$, as revealed in Fig. 12(b). This two-way interaction also affects the power extraction performance of both foils, as will be discussed in the next section.

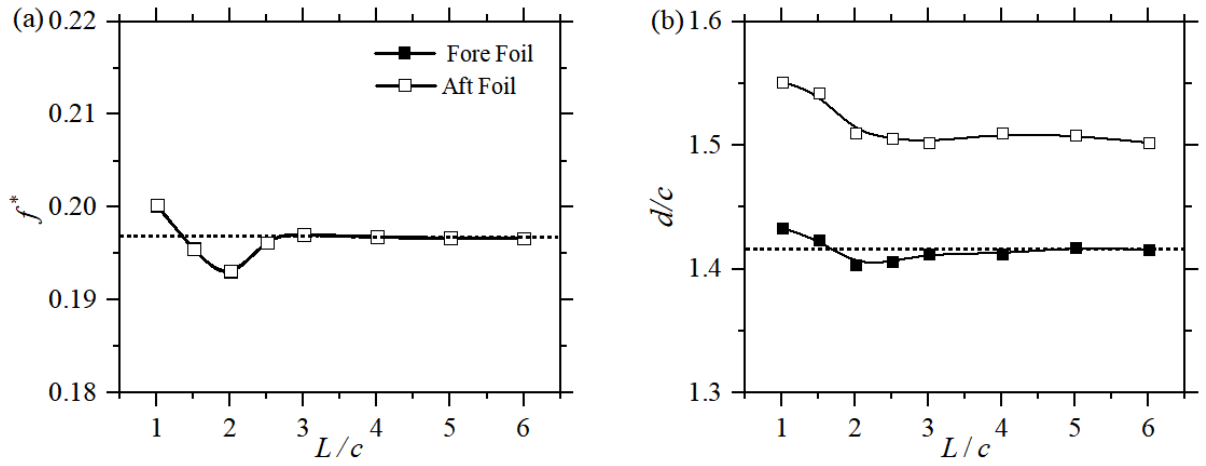

Fig. 12 CFD results of (a) flapping frequency $f^* = fc/U_\infty$ and (b) heaving distance of the two foils against the tandem distance. The dashed lines denote the values for the single foil case.

3.4 Power extraction performance

The overall power coefficients evaluated from CFD simulations are shown in Fig. 13. It reveals that the fore foil is able to extract the maximum mean heaving power of $\overline{C}_{ph} = 0.223$ when the two foils are closest, i.e., $L = c$. $\overline{C}_{ph}$ quickly reduces with the tandem distance, reaching its minimum value 0.177 at $L = 2c$. As the tandem distance further increases, $\overline{C}_{ph}$ rebounds and gradually approaches to the value for the single foil (i.e., 0.193). As for the mean pitching power $\overline{C}_{p\theta}$, it monotonically increases with the tandem distance from its minimum

value 0.022 at $L = c$ and gradually approaches to the value of the single foil (i.e., 0.045). Since the variation in $\bar{C}_{ph}$ is larger than that in $\bar{C}_{p\theta}$, their summation, the mean total power $\bar{C}_p$, shows a similar variation trend with $\bar{C}_{ph}$. That is, as L increases from c, $\bar{C}_p$ decreases first and then gradually increases to approach to its single-foil value 0.238, leaving a trough at $L = 2c$.

Influenced by the fore foil's wake, the aft foil is able to extract in average 10.4% more heaving power $\bar{C}_{ph}$ than the single foil. This wake-foil interaction benefit could be more significant for the pitching power. With the smallest tandem distance, i.e., $L = c$, the aft foil can extract about twice the pitching power $\bar{C}_{p\theta}$ of the single foil. Unfortunately, this power surplus quickly reduces to almost nothing as L increases to just $2c$. When the two foils are sufficiently far from each other, i.e., $L > 3c$, the aft foil's pitching power extraction achieves a stable performance, which is about 20% more than the single foil. As such, the mean total power $\bar{C}_p$ for the aft foil is in average about 15.2% larger than the single foil and the fore foil, showing a similar variation trend as $\bar{C}_{p\theta}$.

The power conversion efficiency for both the foils, η, follows similar trends of the respective $\bar{C}_p$, as shown in Fig. 13(b). The maximum efficiency 19.6% is achieved by the aft foil at $L = c$, whereas the minimum efficiency 15.9% is achieved by the fore foil at $L = 2c$. By adding the efficiencies of both foils, the total efficiency of the tandem foil system is in average 1% higher than twice the single foil's efficiency. The maximum total efficiency of 36.8% is achieved at $L = c$, the shortest tandem distance the two foils can be arranged. In practice, however, at this extreme condition the two foils may collide due to the assembly tolerance.

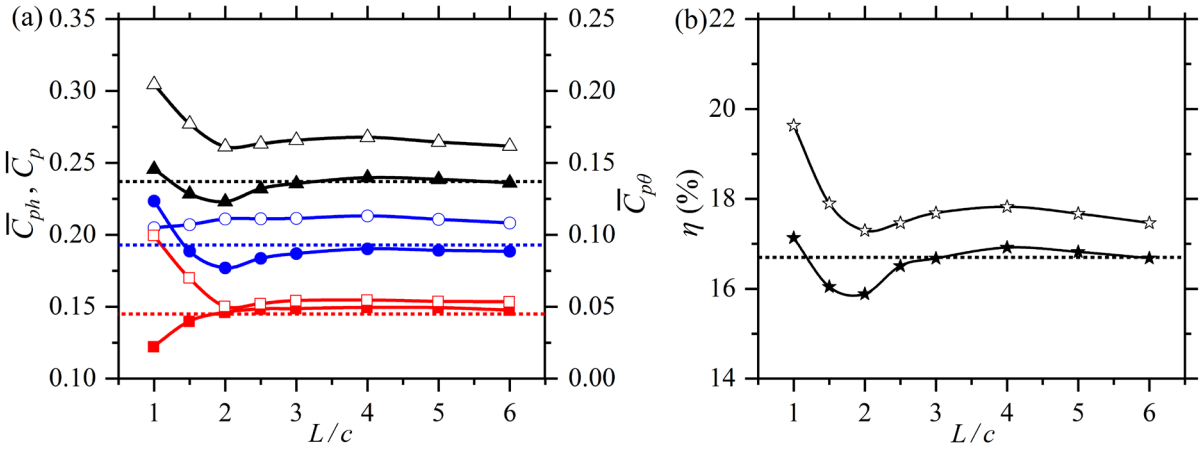

Fig. 13 CFD simulated flow power extraction performance: (a) power coefficients and (b) power conversion efficiency. All solid symbols are data for the fore foil, all open symbols are data for the aft foil, and all dash lines are values for the single foil. Blue circles – mean heaving power coefficients $\bar{C}_{ph}$, red squares – mean pitching power coefficients $\bar{C}_{p\theta}$, black triangles – total power coefficients $\bar{C}_p$, and black stars – power conversion efficiency η.

3.5 Key dynamics of the fore foil

To pin down the reasons behind the variations in the mean power coefficients and their differences observed in Fig. 13, the simulated one-flapping-cycle evolution of the fore foil's displacements, velocities, force/moment and power coefficients for three representative cases, i.e., $L = c$, $2c$ and $4c$, as well as the single foil case are presented and compared in Fig. 14. Since the $L = c$ case (red line) has the highest frequency (evidenced in Fig. 12(a)) and hence the largest inertial force, it exhibits the largest heaving amplitude as shown in Fig. 14(a). On the contrary, the $L = 2c$ case (green line) has the lowest frequency and hence the smallest inertial force, so it exhibits the smallest heaving amplitude among all selected cases.

It is seen from Fig. 14(d) that the larger mean heaving power $\bar{C}_{ph}$ in the $L = c$ case is mainly contributed in the second half ($t/T = 0.7 \sim 0.83$ or $0.2 \sim 0.33$) of the pure heaving phase (with white background), where the heaving force C_h is significantly larger than those in the other cases and the heaving velocity $\dot{h}$ is at a high level in the same direction (see Fig. 14(c)). This significantly enhanced heaving force is caused by the fast rotation of the aft foil when the two foils become close, which results in a clear fling motion between the two foils and generates a prominent low-pressure region right on the fore foil's suction surface, as shown by the flow and

pressure fields at t/T = 0.7 (or 0.2) in Fig. 15(b2). Meanwhile, during this period the aft foil undergoes the pitching motion in the near-wall region, which increases the blockage to the water channel and hence leads to increased pressure on the fore foil's pressure surface, as evidenced in Fig. 15(b2) and (b3). These two factors collectively increase the heaving force experienced by the fore foil, hence contributing to the exceptionally high mean heaving power $\overline{C}_{ph}$ in the $L = c$ case as observed in Fig. 13(a).

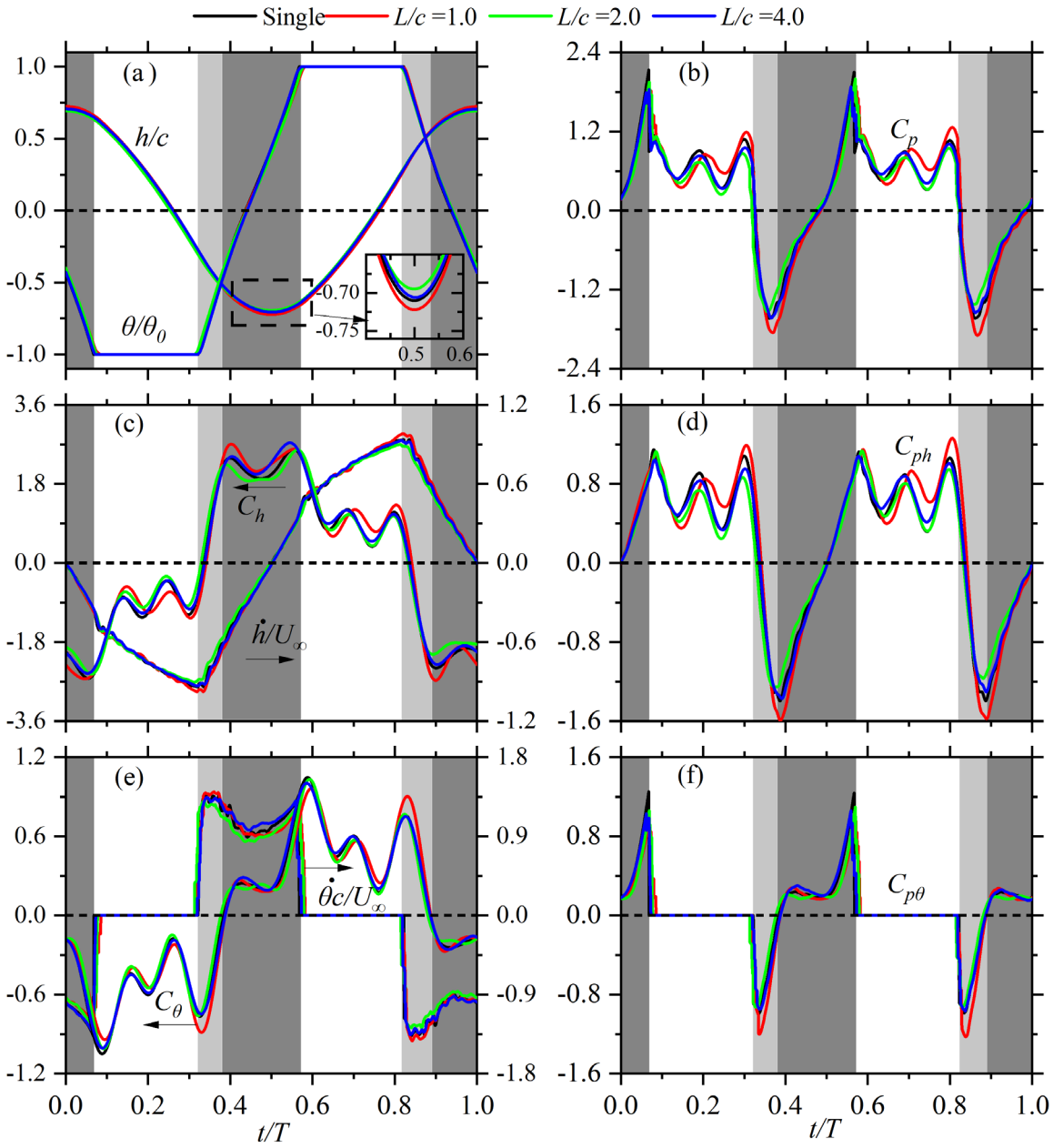

Fig. 14 Evolution of (a) the heaving and pitching displacements, (b) the total power coefficients, (c) the heaving force coefficient and velocity, (d) the heaving power coefficient, (e) the pitching moment coefficient and velocity, and (f) the pitching power coefficient of the fore foil in three representative tandem-foil cases and the single-foil case. The white, light grey and dark grey backgrounds denote the pure heaving phase, the sliding stage of the stroke reversal phase, and the free stage of the stroke reversal phase, respectively, in the single-foil case.

From Fig. 14(f), a much larger negative pitching power $C_{p\theta}$ is observed in the $L = c$ case at around t/T = 0.85 (or 0.35) in the sliding stage (with light grey background). Around this instant, the fore foil just finishes its pure heaving phase with a larger heaving velocity $\dot{h}$ which is then converted into a larger pitching velocity $\dot{\theta}$, as evidenced in Figs. 14(c) and (e). The faster heaving and pitching motions generate a significantly larger reaction torque C_θ as shown in Fig. 14(e), which stems from the much higher pressure generated in the region between

the trailing edge of the fore foil and the channel wall, as shown in Fig. 15(b4). It is this large reaction torque that generates large negative power, contributing to the significantly low mean pitching power $\bar{C}_{p\theta}$ observed in the $L = c$ case. Furthermore, the high pressure between the trailing edge of the fore foil and the channel wall lasts for a short while (Figs. 15(b4) and (b5)) during the rotation of the fore foil, which is responsible for the higher heaving force (C_h in Fig. 14(c)) and the resulting larger heaving power consumption (C_{ph} in Fig. 14(d)) observed at about $t/T = 0.9$ (or 0.4).

As for the minimum mean heaving power $\bar{C}_{ph}$ appearing in the $L = 2c$ case, Fig. 14(d) reveals that it is mainly attributed to the worsened power extraction performance during $t/T = 0.65$ to 0.75 (or 0.15 to 0.25) in the pure heaving phase (with white background). Fig. 14(c) further reveals that this worsened performance is due to the slight reduction of the heaving force C_h. Close inspection of the velocity and pressure fields suggests that this slight force reduction is caused by the influence from the aft foil. Since in this case the two foils are nearly antiphase, when the fore foil is about to reach the centerline of the channel, e.g., at $t/T = 0.7$ (or 0.2) as shown in Fig. 15(c2), the aft foil is also about to reach the centerline from the opposite side. Around this instant, the blockage caused by the downstream aft foil induces higher pressure on the suction surface of the fore foil, resulting in the slight reduction in the heaving force.

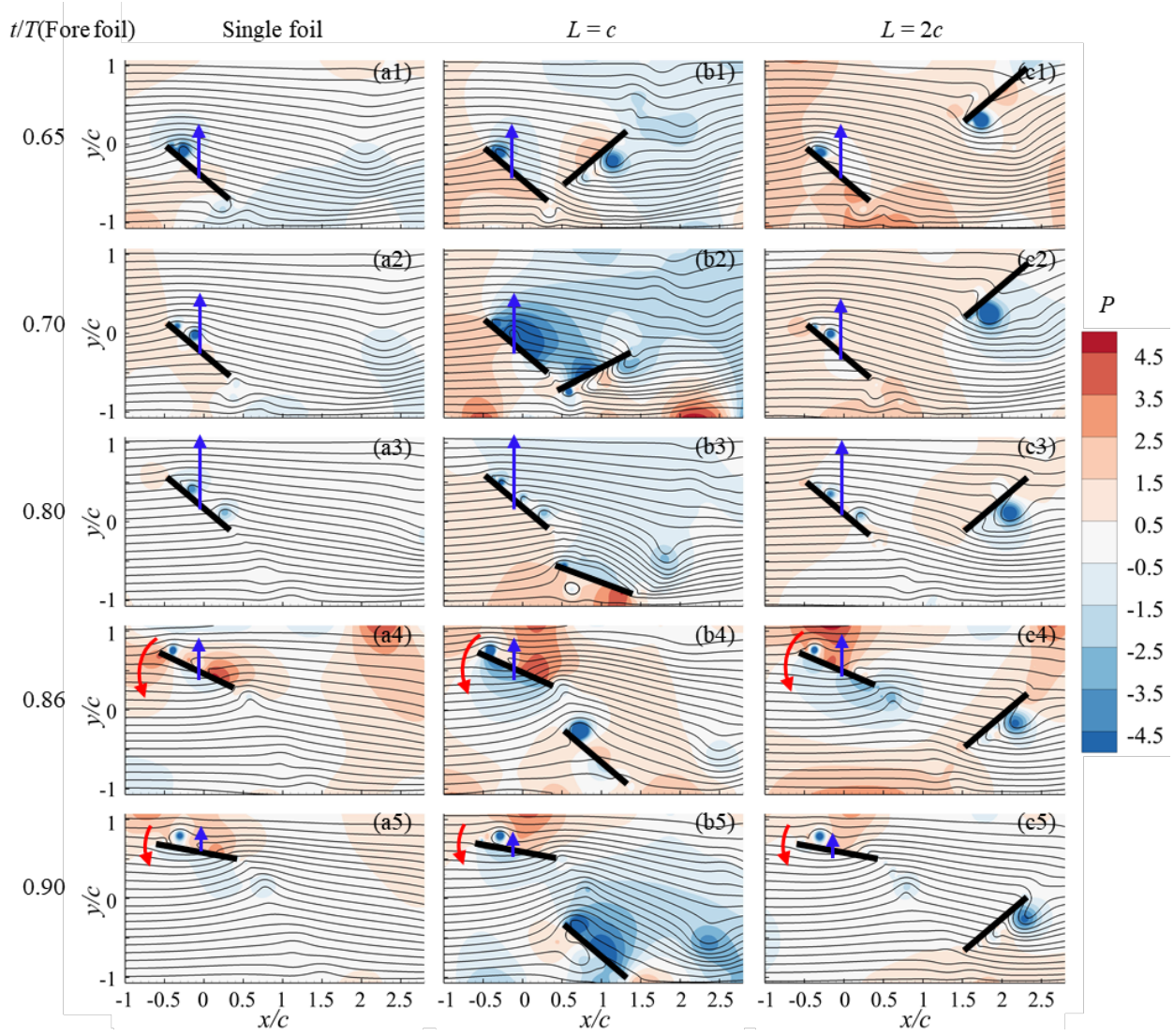

Fig. 15 Snapshots of flow and pressure fields when the fore foil undergoes the upstroke. The flow comes from the left side. Blue arrows indicate the heaving motion, and red arrows indicate the pitching motion, and its length is to express the magnitude.

3.6 Key dynamics of the aft foil

Fig. 16 compares the one-cycle evolution of the aft foil's displacements, velocities, force/moment and power coefficients for the same three selected cases, i.e., $L = c$, $2c$ and $4c$, as well as the single foil case. Note that, different from Fig. 14, the start of the flapping cycle in these plots is adjusted according to the aft foil's kinematics to facilitate easy comparison. As revealed in Fig. 16(a), in all the tandem foil cases the aft foil shows a larger (by about 7.1% in average) heaving amplitude than that in the single case, which has already been presented in Fig. 12(b), and its stroke reversal phase also ends earlier. Considering their mildly varying

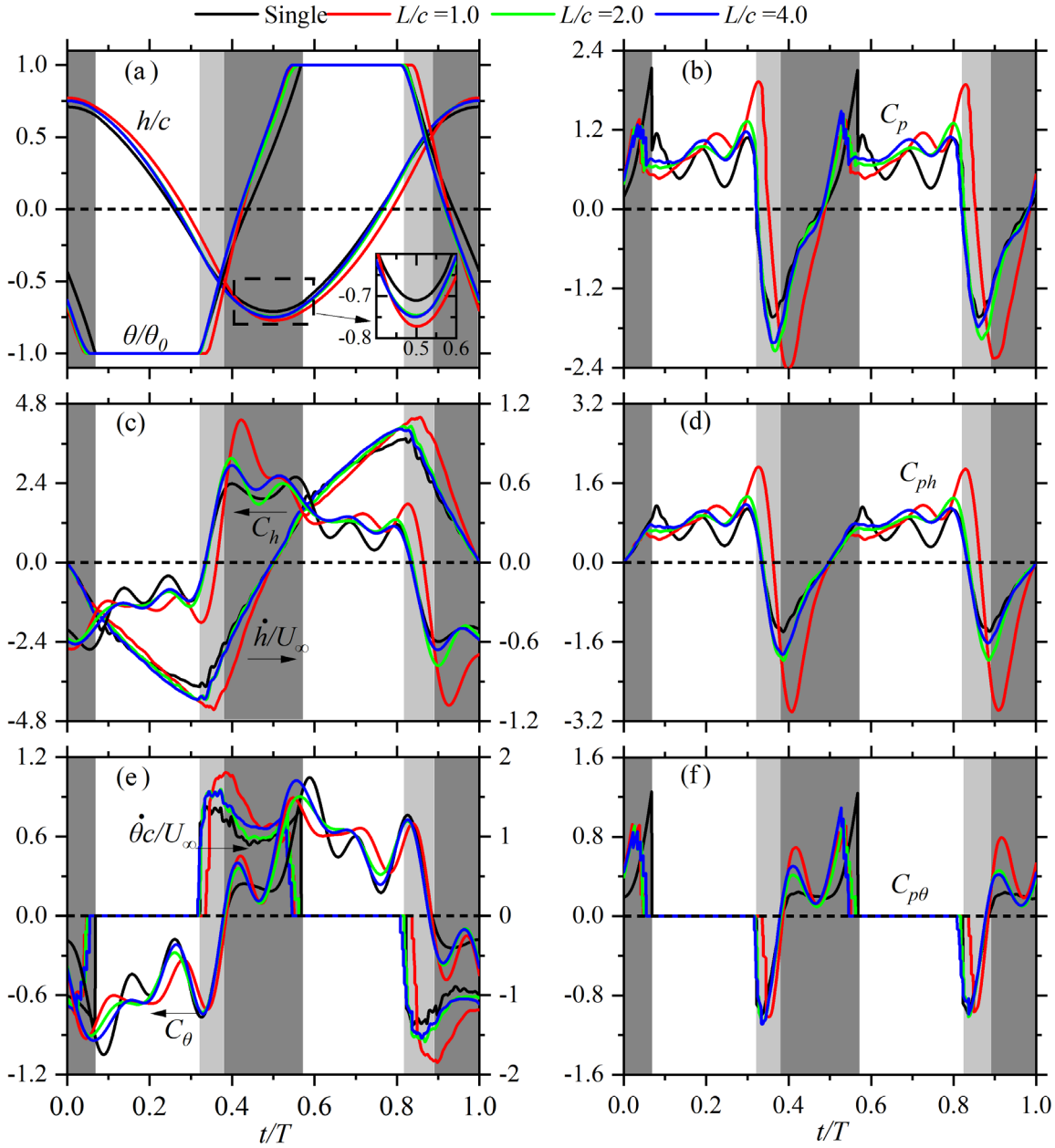

Fig. 16 Evolution of (a) the heaving and pitching displacements, (b) the total power coefficients, (c) the heaving force coefficient and velocity, (d) the heaving power coefficient, (e) the pitching moment coefficient and velocity, and (f) the pitching power coefficient of the aft foil in three representative tandem-foil cases and the single-foil case. The white, light grey and dark grey backgrounds denote the pure heaving phase, the sliding stage of the stroke reversal phase, and the free stage of the stroke reversal phase, respectively, in the single-foil case.

frequencies (see Fig. 12(a)), this suggests that the aft foil must experience higher heaving and pitching velocities, which also reflects that, for the same foil system, generally higher heaving force C_h and pitching moment C_θ are experienced by the aft foil, as confirmed in Figs.16(c) and (e). As such, it is not surprising to see that the aft foil can extract in average 10% more mean heaving power $\bar{C}_{ph}$, mean pitching power $\bar{C}_{p\theta}$ and

total power $\bar{C}_p$ than the single foil, as having already been shown in Fig. 13(a).

From Fig. 16(c), it is seen that the heaving force C_h in the $L = c$ case is significantly high during t/T = 0.8 to 1.0 (or 0.3 to 0.5) when the aft foil undergoes the stroke reversal, subsequently showing one positive spike and one negative spike. Initially, this high heaving force around the first spike (denoted as the first C_h peak) pushes the aft foil very hard towards the wall, causing a high heaving velocity $\dot{h}$ in the same direction and hence generating a high peak of the heaving power C_{ph} at $t/T = 0.83$ (or 0.33), as evidenced in Fig. 16(d). Then, this heaving force reverses its direction and quickly forms the negative spike (denoted as the second C_h peak) at $t/T = 0.91$ (or 0.41). This reversed heaving force is applied to the heaving velocity in the opposite direction, causing the aft foil to fast decelerate and eventually reverse its heaving direction at about $t/T = 0.5$ (or 1.0). As such, a huge power consumption occurs, which greatly compensates the extracted power during the pure heaving phase. This explains in this case why the mean heaving power extraction performance is not prominent, as observed in Fig. 13(a), despite its fastest flapping motion.

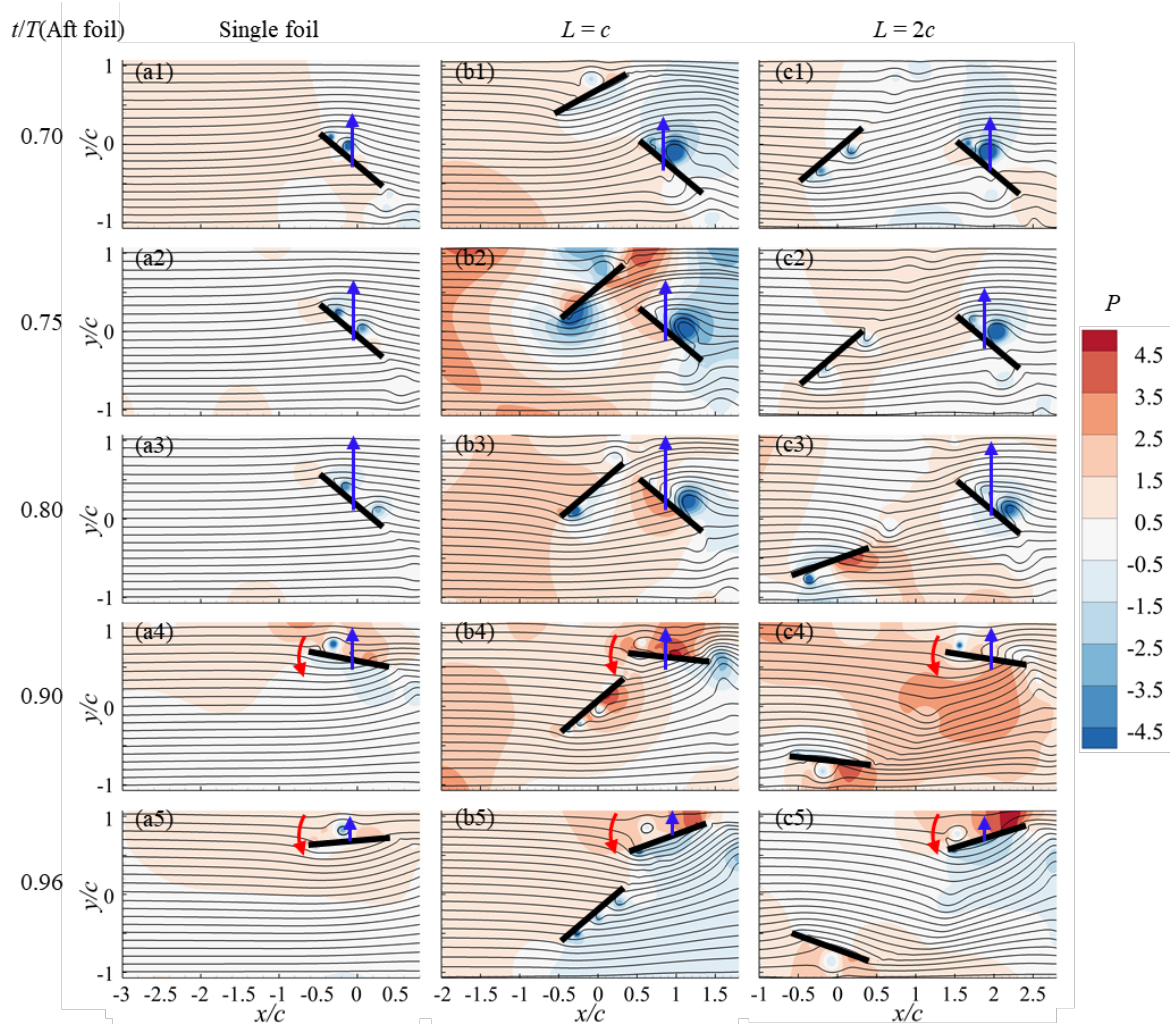

Fig. 17 Snapshots of flow and pressure fields when the aft foil undergoes the upstroke. The flow comes from the left side. Blue arrows indicate the heaving motion, and red arrows indicate the pitching motion, and its length is to express the magnitude.

From the flow and pressure fields at selected instants shown in Fig. 17, it is seen that the first C_h peak in the $L = c$ case appearing in Fig. 16(c) is caused by the strong interaction between the two foils. At $t/T = 0.8$ (or 0.3) as shown in Fig. 17(b3), the fore foil just finishes its stroke reversal and starts its pure downward heaving, while the aft foil is about to finish its pure upward heaving and start its stroke reversal due to their $\pi/2$ phase difference. At this instant these two foils are right next to each other with opposite maximum pitching angles,

so that the aft foil captures the high-momentum flow "ejected" through the fast rotation of the fore foil. This high-momentum ejection is clearly evidenced in Figs. 17(b2) and (b3) by the negative pressure on the fore foil's suction surface and the positive pressure on the aft foil's pressure surface. The latter is then responsible for the first C_h peak at $t/T = 0.83$ (or 0.33).

The second C_h peak appears right after the heaving force reverses its direction, which is associated with the strong reaction from the fluid between the aft foil and the channel wall. Since the aft foil has been accelerated to an obviously higher heaving velocity due to the first C_h peak, it pushes the fluid towards the wall much harder, hence inducing a much higher reaction force that leads to the tremendous second C_h peak. This can be evidenced by the prevailing high pressure above the aft foil as shown in Fig. 17(b4), which is quite different from that in the single-foil and $L = 2c$ cases.

The two C_h peaks in the $L = c$ case also contribute to the aft foil's high mean pitching power as observed in Fig. 13(a). The enhanced heaving velocity is quickly converted into an enhanced pitching velocity $\dot{\theta}$ due to the functioning of the heaving limiter, as evidenced in Fig. 16(e) at around $t/T = 0.9$ (or 0.4). In addition, the high pressure above the aft foil, especially at the leading edge as shown in Figs. 17(b4) and (b5), also creates a higher pitching moment C_θ at around $t/T = 0.93$ (or 0.43). These two factors then collectively produce the significantly higher pitching power $C_{p\theta}$ as shown in Fig. 16(f), leading to the high mean pitching power $\bar{C}_{p\theta}$ for the aft foil.

3.7. Wall effects

The above results have revealed that the channel walls played an important role in affecting the dynamics and power extraction performance of the tandem foils. To assess how significant the influence is, we conducted more CFD simulations on selected cases in which the walls were removed. Table 6 compares the system performance with and without the channel walls. It is clearly seen that the walls greatly improve the energy extraction performance, regardless of single case and tandem cases, averagely by about 40% in terms of the total power coefficient $\bar{C}_p$. This is not surprising since many previous works have also revealed similar findings, on fully active (Gauthier et al. 2016; Su et al. 2019) and semi-active flapping foil systems (Wu et al. 2014). The comparison also confirms that, without the walls, the aft foil can still outperform the single and fore foils.

Table 6. Comparison of the system performance with and without channel walls

			$L = c$		$L = 2c$		$L = 4c$	
		Single Foil	Fore Foil	Aft Foil	Fore Foil	Aft Foil	Fore Foil	Aft Foil
Without channel walls	$\varphi/2\pi$	-	0.377		0.600		0.995	
	$\bar{C}_{ph}$	0.142	0.134	0.151	0.137	0.162	0.141	0.175
	$\bar{C}_{p\theta}$	0.037	0.038	0.059	0.034	0.041	0.037	0.033
	$\bar{C}_p$	0.179	0.172	0.211	0.171	0.203	0.178	0.208
	η	12.1%	11.8%	12.7%	11.9%	12.2%	12.1%	12.5%
With channel walls	$\varphi/2\pi$	-	0.328		0.597		1.02	
	$\bar{C}_{ph}$	0.19	0.223	0.205	0.177	0.211	0.19	0.213
	$\bar{C}_{p\theta}$	0.045	0.022	0.1	0.046	0.05	0.049	0.055
	$\bar{C}_p$	0.235	0.246	0.305	0.223	0.261	0.239	0.268
	η	16.7%	17.1%	19.6%	15.9%	17.3%	16.9%	17.8%

The simulation results also reveal that, without the walls, the aft foil can still be modulated by the wake of the fore foil, finally locked to a stable phase difference that is independent of the foils' initial states. This phase difference is nearly unchanged when the walls are removed in the $L = 2c$ and $4c$ cases and only increases by about 15% in the $L = c$ case. This suggests that the Φ and Φ_w values derived in Sec. 3.2 are still valid when the tandem distance is large enough, regardless of the existence of channel walls.

5. Conclusions

We investigated the dynamics and energy harvesting performance of two fully passive flapping foil arranged in tandem in a water channel. Both experimental measurements and CFD simulations are conducted to provide complementing data for the analysis. According to the understanding achieved on the single foil system from our previous studies, the water flow speed is set at $U_\infty = 0.62$ m/s and the foil parameters are set as $x_p = 0.6c$, $\theta_0 = 40°$, $d_h = 1.36c$ and $d_x = 0.46c$. The major findings are as follows:

1. Through the wake-foil interaction, the aft foil can be modulated and eventually locked by the LEV generated from the flapping fore foil, leading to a stable phase difference φ that is independent of their initial states. The wake capture mechanism results in a zero wake phase for the aft foil, which is confirmed by the nearly linear relationship observed between φ and the tandem distance L.
2. Due to the wake-foil interaction, the aft foil exhibits larger heaving and pitch velocities, extracting in average 15.2% more power than the fore foil and the single foil.
3. As $L \geq 3c$, the fore foil behaviors almost the same as the single foil. As $L < 3c$, however, it is affected by the aft foil through two-way interactions. Specifically, its best power extraction occurring at $L = c$ is mainly due to the enhanced heaving force that is caused by the fling motion between the two close-by foils and the channel-wall effect, while its worst power extraction occurring at $L = 2c$ is mainly due to the channel blockage caused by the two foils during pure heaving.
4. The maximum power extraction efficiency of 19.7% is achieved by the aft foil at $L = c$, while the minimum efficiency of 15.9% is achieved by the fore foil at $L = 2c$. The two foils can collectively achieve the best efficiency of 36.8% at $L = c$, more than the doubled value (33.4%) of the single foil's efficiency. Unfortunately, they also collectively achieve the worst efficiency of 33.2% at $L = 2c$. As the two foils are far enough from each other, i.e., $L \geq 3c$, a marginal enhancement of about 1% in the collective efficiency is achieved.
5. Wall effects can significantly improve the energy extraction performance of the system. Regardless of the existence of channel walls, the aft foil can still outperform the single and fore foils, and the Φ and Φ_w values derived in Sec. 3.2 are always valid if the tandem distance is large enough.

Since two or more foils can in general be arranged with a non-zero staggered distance, which will affect the dynamics of the foils especially the aft foil, in the near future we will conduct a further study to investigate its effect.

Acknowledgement

This work is supported by Natural Science Foundation of Guangdong Province (Project No. 2021A1515010337) and partially supported by Natural Science Foundation of China under Training Program of Major Research Plan (Project No. 91952107).

References

[1]. Abdelkefi A. Aeroelastic energy harvesting: A review[J]. International Journal of Engineering Science, 2016, 100: 112-135.

[2]. Abiru H, Yoshitake A. Experimental study on a cascade flapping wing hydroelectric power generator[C]//ASME Power Conference. 2011, 44601: 537-543.

[3]. Ashraf M A, Young J, Lai J C S, et al. Numerical analysis of an oscillating-wing wind and hydropower generator[J]. AIAA journal, 2011, 49(7): 1374-1386.

[4]. Broering T M, Lian Y, Henshaw W. Numerical investigation of energy extraction in a tandem flapping wing configuration[J]. AIAA journal, 2012, 50(11): 2295-2307.

[5]. Broering T M, Lian Y S. The effect of phase angle and wing spacing on tandem flapping wings[J]. Acta Mechanica Sinica, 2012, 28(6): 1557-1571.

[6]. Gauthier E, Kinsey T, Dumas G. Impact of blockage on the hydrodynamic performance of oscillating-foils hydrokinetic turbines[J]. Journal of Fluids Engineering, 2016, 138(9).

[7]. Jones K D, Lindsey K, Platzer M F. An investigation of the fluid-structure interaction in an oscillating-wing micro-hydropower generator[J]. WIT Transactions on The Built Environment, 2003, 71.

[8]. Karbasian H R, Esfahani J A, Barati E. Simulation of power extraction from tidal currents by flapping foil hydrokinetic turbines in tandem formation[J]. Renewable Energy, 2015, 81: 816-824.
[9]. Karakas F, Fenercioglu I. Effect of phase angle on tandem flapping-wing power generation[J]. International Journal of Energy Production and Management. 2017. Vol. 2. Iss. 1, 2017, 2(1): 95-105.
[10]. Kinsey T, Dumas G. Parametric study of an oscillating airfoil in a power-extraction regime[J]. AIAA journal, 2008, 46(6): 1318-1330.
[11]. Kinsey T, Dumas G, Lalande G, et al. Prototype testing of a hydrokinetic turbine based on oscillating hydrofoils[J]. Renewable energy, 2011, 36(6): 1710-1718.
[12]. Kinsey T, Dumas G. Computational fluid dynamics analysis of a hydrokinetic turbine based on oscillating hydrofoils[J]. Journal of fluids engineering, 2012a, 134(2).
[13]. Kinsey T, Dumas G. Optimal tandem configuration for oscillating-foils hydrokinetic turbine[J]. Journal of fluids engineering, 2012b, 134(3).
[14]. Kim J, Le T Q, Ko J H, et al. Experimental and numerical study of a dual configuration for a flapping tidal current generator[J]. Bioinspiration & biomimetics, 2015, 10(4): 046015.
[15]. Liu W. A case study on tandem configured oscillating foils in shallow water[J]. Ocean Engineering, 2017, 144: 351-361.
[16]. Platzer M, Ashraf M A, Young J, et al. Development of a new oscillating-wing wind and hydropower generator[C]. 47th AIAA Aerospace Sciences Meeting including the New Horizons Forum and Aerospace Exposition. 2009a: 1211.
[17]. Ma P, Wang Y, Xie Y, et al. Effect of wake interaction on the response of two tandem oscillating hydrofoils[J]. Energy Science & Engineering, 2019, 7(2): 431-442.
[18]. Ma P, Wang Y, Xie Y, et al. Behaviors of two semi-passive oscillating hydrofoils with a tandem configuration[J]. Energy, 2021, 214: 118908.
[19]. Platzer M F, Bradley R A. Oscillating-wing power generator with flow-induced pitch-plunge phasing. US Patent Pub. No. US20090121490A1, 2009b.
[20]. Platzer M, Sarigul-Klijn N. A novel approach to extract power from free-flowing water and high altitude jet streams[C]. Energy Sustainability. 2009c, 48890: 493-499.
[21]. Pourmahdavi M, Liu P. Shallow water effect of tandem flapping foils on renewable energy production[J]. International Journal of Green Energy, 2019, 16(14): 1353-1362.
[22]. Qadri M N M, Zhao F, Tang H. Fluid-structure interaction of a fully passive flapping foil for flow energy extraction[J]. International Journal of Mechanical Sciences, 2020, 177: 105587.
[23]. Ribeiro B L R, Su Y, Guillaumin Q, et al. Wake-foil interactions and energy harvesting efficiency in tandem oscillating foils[J]. Physical Review Fluids, 2021, 6(7): 074703.
[24]. Su Y, Miller M, Mandre S, et al. Confinement effects on energy harvesting by a heaving and pitching hydrofoil[J]. Journal of Fluids and Structures, 2019, 84: 233-242.
[25]. Wang J, Geng L, Ding L, et al. The state-of-the-art review on energy harvesting from flow-induced vibrations[J]. Applied Energy, 2020, 267: 114902.
[26]. Wang J, Gu S, Zhang C, et al. Hybrid wind energy scavenging by coupling vortex-induced vibrations and galloping[J]. Energy Conversion and Management, 2020, 213: 112835.
[27]. Wang J, Zhao L. Toward nonlinear galloping energy harvesting interfaced with different power extraction circuits[J]. IEEE/ASME Transactions on Mechatronics, 2021.
[28]. Wu J, Qiu Y L, Shu C, et al. Pitching-motion-activated flapping foil near solid walls for power extraction: A numerical investigation[J]. Physics of Fluids, 2014, 26(8): 083601.
[29]. Wu J, Qiu Y L, Shu C, et al. Pitching-motion-activated flapping foil near solid walls for power extraction: A numerical investigation[J]. Physics of Fluids, 2014, 26(8): 083601.
[30]. Wu X, Zhang X, Tian X, et al. A review on fluid dynamics of flapping foils[J]. Ocean Engineering, 2020, 195: 106712.
[31]. Xiao Q, Zhu Q. A review on flow energy harvesters based on flapping foils[J]. Journal of fluids and structures, 2014, 46: 174-191.
[32]. Xu J, Sun H, Tan S. Wake vortex interaction effects on energy extraction performance of tandem oscillating hydrofoils[J]. Journal of Mechanical Science and Technology, 2016, 30(9): 4227-4237.
[33]. Xu J, Tan S, Guan D, et al. Energy extraction performance of motion-constrained tandem oscillating hydrofoils[J]. Journal of Renewable and Sustainable Energy, 2017, 9(4): 044501.
[34]. Xu G D, Xu W H. Energy extraction of two flapping foils with tandem configurations and vortex interactions[J]. Engineering Analysis with Boundary Elements, 2017, 82: 202-209.
[35]. Xu W, Xu G, Duan W, et al. Experimental and numerical study of a hydrokinetic turbine based on tandem flapping hydrofoils[J]. Energy, 2019, 174: 375-385.
[36]. Young J, Lai J C S, Platzer M F. A review of progress and challenges in flapping foil power generation[J]. Progress in aerospace sciences, 2014, 67: 2-28.
[37]. Zhao F, Qadri M N M, Wang Z, et al. Flow-energy harvesting using a fully passive flapping foil: A guideline on

design and operation[J]. International Journal of Mechanical Sciences, 2021, 197: 106323.